ADVANCED MATERIALS
www.advmat.de

Stimuli-Responsive Liquid-Crystal-Infused Porous Surfaces for Manipulation of Underwater Gas Bubble Transport and Adhesion

Adil Majeed Rather, Yang Xu, Yun Chang, Robert Lewis Dupont, Angana Borbora, Ufuoma Israel Kara, Jen-Chun Fang, Rajdeep Mamtani, Meng Zhang, Yuxing Yao, Solomon Adera, Xiaoping Bao, Uttam Manna,* and Xiaoguang Wang**

Biomimetic artificial surfaces that enable the manipulation of gas bubble mobility have been explored in a wide range of applications in nanomaterial synthesis, surface defouling, biomedical diagnostics, and therapeutics. Although many superhydrophobic surfaces and isotropic-lubricant-infused porous surfaces have been developed to manipulate gas bubbles, the simultaneous control over the adhesion and transport of gas bubbles underwater remains a challenge. Thermotropic liquid crystals (LCs), a class of structured fluids, provide an opportunity to tune the behavior of gas bubbles through LC mesophase transitions using a variety of external stimuli. Using this central idea, the design and synthesis of LC-infused porous surfaces (LCIPS) is reported and the effects of the LC mesophase on the transport and adhesion of gas bubbles on LCIPS immersed in water elucidated. LCIPS are demonstrated to be a promising class of surfaces with an unprecedented level of responsiveness and functionality, which enables the design of cyanobacteria-inspired object movement, smart catalysts, and bubble gating devices to sense and sort volatile organic compounds and control oxygen levels in biomimetic cell cultures.

1. Introduction

The manipulation of gas bubbles in aqueous environments is frequently observed on biological surfaces in a variety of functions. For example, the hydrophobic nanostructured microfibers on the bodies of great diving beetles (e.g., *Dytiscus marginalis*)[1] and diving bell spiders (e.g., *Argyroneta aquatic*)[2] can efficiently adhere and immobilize air bubbles to provide the oxygen necessary for their survival underwater. Another prominent example is the gas bubble-assisted buoyancy regulation by cyanobacteria. *Anabaena Flos-Aquae*, a freshwater cyanobacteria species, have assemblies of hydrophobic proteins, namely gas vesicles, within them that can dynamically adhere and release gas bubbles inside their cells to control their depth in lakes.[3] To date, a number of applications based on gas bubbles have

A. M. Rather, Y. Xu, R. L. Dupont, U. I. Kara, J.-C. Fang, R. Mamtani, M. Zhang, X. Wang
William G. Lowrie Department of Chemical and Biomolecular Engineering
The Ohio State University
Columbus, OH 43210, USA
E-mail: wang.12206@osu.edu

Y. Chang, X. Bao
Davidson School of Chemical Engineering
Purdue Center for Cancer Research
Purdue University
West Lafayette, IN 47907, USA
E-mail: bao61@purdue.edu

A. Borbora, U. Manna
Bio-Inspired Polymeric Materials Lab
Department of Chemistry
Indian Institute of Technology-Guwahati
Kamrup, Assam 781039, India
E-mail: umanna@iitg.ac.in

Y. Yao
Division of Chemistry and Chemical Engineering
California Institute of Technology
Pasadena, CA 91125, USA

S. Adera
Department of Mechanical Engineering
University of Michigan
Ann Arbor, MI 48109, USA

U. Manna
Centre for Nanotechnology
Indian Institute of Technology-Guwahati
Kamrup, Assam 781039, India

X. Wang
Sustainability Institute
The Ohio State University
Columbus, OH 43210, USA

The ORCID identification number(s) for the author(s) of this article can be found under https://doi.org/10.1002/adma.202110085.

DOI: 10.1002/adma.202110085

emerged that rely on the on-demand adhesion and transport of gas bubbles underwater, including surface defouling,[4] site-specific biological imaging,[5] targeted gas delivery for therapeutics,[6] hydrodynamic drag reduction,[7] and critical heat flux enhancement in heat transfer.[8] Researchers have developed biomimetic artificial surfaces, including superhydrophobic metal wires,[9] cotton yarn,[10] and synthetic polymeric sheets[11] with micro- or nanostructures that can strongly immobilize gas bubbles underwater. However, the strong adhesion to gas bubbles exhibited by these superhydrophobic surfaces impedes the pinning-free transport of bubbles on the interfaces,[12] which limits their use in applications requiring facile bubble transport, such as oxygen delivery.

Recently, another class of bioinspired functional surfaces have been developed for use in applications requiring facile bubble transport, namely slippery liquid-infused porous surfaces (SLIPS), which mimic the lubricant-infused nanoporous structures of the pitcher plant (*Nepenthes alata*).[13] The isotropic-lubricant-based SLIPS, which typically uses silicone oil or perfluorinated oil as lubricants, possess numerous advantages over superhydrophobic surfaces, including excellent liquid repellency at high pressure,[14] good stability underwater,[14] and a remarkably facile transport of underwater gas bubbles.[15] Past studies have reported that magnetic fields and mechanical stretching can be used to change the surface topography of the solid substrate coated with SLIPS, resulting in the reversible pinning and sliding of gas bubbles.[16] However, the effects of the properties of these isotropic lubricants (e.g., molecular order and phase behaviors) on the dynamics of underwater gas bubbles on SLIPS have not been fully understood,[17] and the design of anisotropic- and structured-liquid-based SLIPS capable of the on-demand immobilization, transport, and release of underwater gas bubbles as a response to a variety of stimuli has not been thoroughly investigated.

Thermotropic liquid crystals (LCs) are anisotropic fluids with unique properties that emerge from the ordered packing of constituent molecules (mesogens), whose long-range orientational order and positional order show responsiveness to external stimuli.[18,19] Although their intrinsic stimuli-responsiveness has been explored to design smart LC surfaces with applications ranging from control over colloidal particle positioning[20] to gas sensors for the detection of nitrogen dioxide, carbon dioxide, and dimethyl methylphosphonate (a simulant of sarin nerve gas),[21] the manipulation of underwater air or gas bubbles on LC surfaces has not yet been explored. Here we report the design of LC-infused porous surfaces (LCIPS) capable of combining the merits of both superhydrophobic surfaces and SLIPS to achieve the on-demand adhesion, transport, and release of gas bubbles on LCIPS via a transition of the LC mesophase using external stimuli such as heat, light, and the presence of chemical species. Based on this intrinsic stimuli-responsiveness, we developed an LCIPS-based bubble gating system that can reversibly activate and deactivate the transport and release of gas bubbles. Additionally, by taking advantage of the buoyancy force associated with bubbles on LCIPS, we demonstrate that the bubbles can lift up and tilt up objects, which can lead to mechanical and chemical applications of the LCIPS, for example, mediating origami box folding and catalytic reactions. More importantly, we demonstrate that volatile organic compound (VOC)-containing gas bubbles can be sensed and sorted from air bubbles using LCIPS, and that LCIPS can be used to regulate oxygen levels in cell cultures to better mimic the hypoxic tumor microenvironment in vivo. Our results will open new possibilities for the design of responsive and multifunctional surfaces for applications ranging from gas bubble microrobotics and VOC sensing and separation to tumor biology studies and effective therapeutic discovery.

2. Results and Discussion

In this work, we selected 4′-octyl-4-biphenylcarbonitrile (8CB) as the LC material for the LCIPS because of its intrinsic temperature-dependent mesophases. Below 25 °C, the 8CB molecules orient themselves in the smectic A phase, with mesogens positionally aligned into stacked layers along one direction. Between 33 and 40 °C, the 8CB mesogens exist in the nematic phase, with mesogens randomly distributed in space with a long-range orientational order (**Figure 1**a). To prepare the LCIPS, we mixed 8CB (90 wt%) with a reactive LC monomer, 1,4-bis-[4-(3-acryloyloxypropyloxy)benzoyloxy]-2-methylbenzene (RM257, 10 wt%), and a photo-initiator, 2,2-dimethoxy-2-phenylacetophenone (1 wt% based on the total mass of the LC) in toluene. After evaporating the toluene, the mixture was placed on a dimethyloctadecyl[3-(trimethoxysilyl) propyl]ammonium chloride (DMOAP)-functionalized glass substrate, followed by polymerization under 365 nm-wavelength UV light for 20 min (see Supporting Information). After polymerization, the 8CB-swelled polyRM257 network was formed, and the resulting porous polymeric structure was verified using scanning electron microscopy analysis (Figure S1, Supporting Information). Finally, LCIPS were obtained by spin coating an ≈130 µm-thick 8CB film on the obtained 8CB-swelled polyRM257 coating. We verified that our 8CB/polyRM257-based LCIPS satisfy the criteria of a stable SLIPS, suggesting that polyRM257 can stabilize 8CB against dewetting caused by water (see Supporting Information).

After the synthesis, we immersed the LCIPS in water and placed air bubbles on the surface to analyze the mesogenic orientation of the underwater air–8CB interface using polarized light microscopy. As shown in Figure 1b, when the 8CB is in the nematic phase (35 °C), the LCIPS appears bright when in contact with the water and dark when in contact with the air bubble. This result implies parallel and perpendicular anchorings of the nematic 8CB at the water–8CB and air–8CB interfaces, respectively. We note here that the DMOAP functionalization induces a perpendicular ordering of the 8CB at the glass substrate.[22] For smectic A 8CB (25 °C), focal conic domains were observed when in contact with water, suggesting a parallel and a perpendicular anchoring of the 8CB at the water–8CB interface and 8CB–polyRM257-coated glass substrate, respectively (Figure S2, Supporting Information). Moreover, we measured the apparent contact angle of the air bubbles to be ≈68° on the LCIPS in both the nematic and smectic A phases ranging from 25 to 40 °C (Figure S3, Supporting Information). We note here that the presence of a LC wetting ridge and a LC wrapping layer around the gas bubble may introduce certain

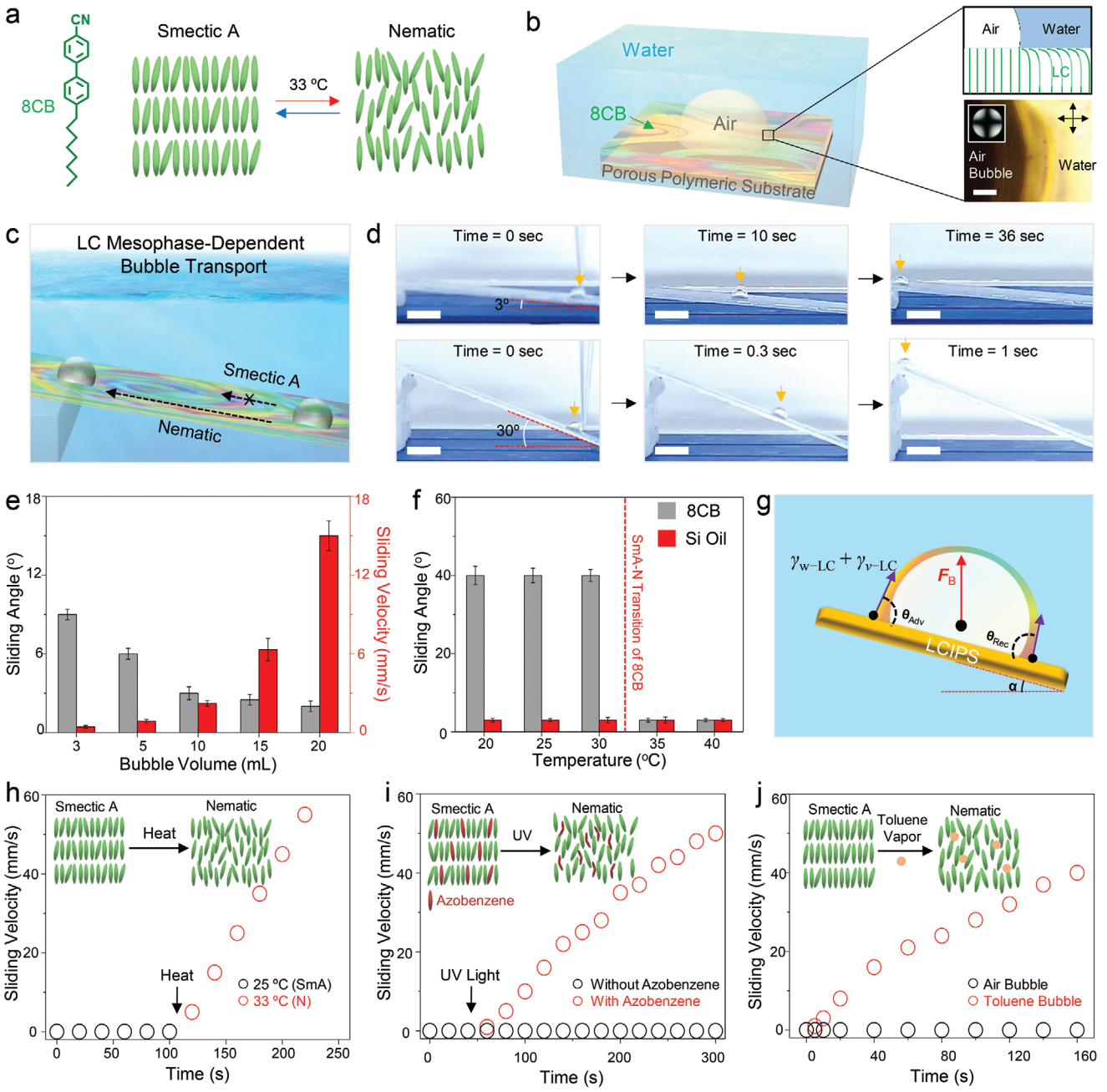

Figure 1. Design of LCIPS for the controlled manipulation of underwater gas bubbles. a) Chemical structure and mesophase transition of 8CB. b) Schematic illustration of an air bubble on an underwater LCIPS. The insets in (b) show the scheme (side view) and corresponding polarized light micrograph (top view) of a 10 µL air bubble on a nematic phase LCIPS. The dark cross pattern in the conoscopic image indicates a uniform perpendicular anchoring of the 8CB in the LCIPS. The double-headed arrows indicate the orientation of the crossed polarizers. Scale bar = 50 µm. c) Schematic illustration of LC-mesophase-dependent bubble transport on a tilted LCIPS. d) Photographs depicting the sliding behavior of 10 µL air bubbles on a tilted LCIPS in the nematic phase. Scale bars = 5 mm. The yellow arrows indicate the position of the air bubbles on the LCIPS. e) Influence of bubble volume on the sliding angle and average sliding velocity of a bubble on a nematic phase LCIPS at a tilting angle of 5°. f) Sliding angle of a 10 µL bubble on an LCIPS and a silicone-oil-based SLIPS (viscosity of silicone oil is ≈20 cSt) as a function of temperature. g) Schematic illustration showing the dominating forces during the sliding of a bubble on an LCIPS. h–j) Activated transport of 10 µL gas bubbles on the LCIPS using heat (h), 365 nm-wavelength UV radiation (i), and toluene vapor (j). The tilting angle of the LCIPS is 5° (h), 10° (i), and 30° (j). For the UV-light-activated transport of air bubbles, the LCIPS was doped with 5 wt% of azobenzene based on the mass of 8CB. Time = 0 s in (h)–(j) indicates the time when a bubble was placed on the LCIPS.

experimental discrepancies in the measurement of the actual contact angle of the air bubbles on the LCIPS, which has been commonly observed in isotropic-oil-based SLIPS.[13] Overall, these results suggest that the intrinsic long-range orientational ordering of the LCs enables the LCIPS to respond optically to the presence of air bubbles.

Next, we investigated the transport of gas bubbles on the LCIPS. As shown in Figure 1c,d, on the nematic phase LCIPS, a 10 µL air bubble can slide at a very low tilting angle (≈3°), and the average sliding velocity of the bubble increases from ≈1 to ≈33 mm s^{-1} with a corresponding increase in the tilting angle from ≈3° to ≈30° (Figure S4, Supporting Information). The average sliding velocity of bubbles on the LCIPS was calculated by dividing the total displacement by the total time of sliding. Moreover, the sliding angle and average sliding velocity of the gas bubble depend on the bubble volume. For example, a 3 µL bubble at a 9° inclination slides at 0.5 mm s^{-1}, while a 20 µL bubble at a 2° inclination slides at 15 mm s^{-1}, as seen in Figure 1e. These results indicate that nematic LCIPS possess a pinning-free slippery behavior that is consistent with isotropic-oil-based SLIPS, as seen in Figure 1f. In contrast to the low sliding angle of ≈3° for 10 µL bubbles on a nematic LCIPS (35 °C), the sliding angle of a 10 µL bubble on a smectic A LCIPS (25 °C) is ≈40°, as shown in Figure 1f. The intrinsically high sliding angle on a smectic A LCIPS implies a high pinning force of gas bubbles similar to the behavior of gas bubbles on superhydrophobic surfaces. In addition, we observed a constant sliding angle for each LC mesophase, even across multiple temperatures within the same mesophase, which is comparative to the temperature-independent bubble transport on the silicone-oil-based SLIPS as shown in Figure 1f. These results lead us to conclude that the transport of gas bubbles on the LCIPS strongly depends on the LC mesophase rather than on the system's temperature.

The sliding of an air bubble on a tilted LCIPS can be described by balancing the buoyancy force of the bubble and the friction force from the LC:

$$\Delta\rho g V \sin\alpha = 2r\left(\gamma_{w-LC} + \gamma_{v-LC}\right)\left(\cos\theta_{Rec} - \cos\theta_{Adv}\right) \quad (1)$$

where $\Delta\rho$ is the mass density difference between air and water, g is the acceleration due to gravity, V is the volume of the bubble, α is the sliding angle of the LCIPS, γ_{w-LC} is the water–LC surface tension, γ_{v-LC} is the air–LC surface tension, r is the base radius of the gas bubble on the LCIPS, and θ_{Adv} and θ_{Rec} are the advancing and receding contact angles, respectively. We note here that the use of "$\gamma_{w-LC} + \gamma_{v-LC}$" instead of the surface tension of water (γ_{v-w}) is because of the formation of a LC wrapping layer around the bubble on the LCIPS (Figure 1g and Supporting Information). Using Equation (1), we calculated the contact angle hysteresis (CAH) of air bubbles (defined as "$\cos\theta_{Rec} - \cos\theta_{Adv}$") to be extremely small (0.03) on a nematic phase LCIPS, while comparatively large (0.29) on a smectic A LCIPS (Figure S5, Supporting Information). We hypothesize that the high surface roughness of smectic A 8CB induces larger CAH and more severe pinning of air bubbles relative to those observed in the nematic phase, which is consistent with our observations of the pinning of water droplets on LC surfaces in different LC mesophases (see Supporting Information for details).[23]

We demonstrate that the LC-mesophase-dependent manipulation of gas bubbles on LCIPS provides a platform by which the immobilization and transport of the bubble can be controlled by inducing a smectic A–nematic transition using external stimuli. For instance, a 10 µL bubble remained immobile on a smectic A LCIPS (25 °C) for 6 h but abruptly began to slide upon heating the LC to the nematic phase (33 °C), as shown in Figure 1h, and Figure S6a and Movie S1, Supporting Information. Beyond heat, we sought to explore other stimuli to activate the transport of bubbles on the LCIPS. To remotely manipulate the motion of gas bubbles on LCIPS, we added azobenzene to the 8CB at 5 wt%. As shown in Figure 1i and Figures S6b,c and S7, Supporting Information, the alternative exposure of 365 nm-wavelength UV light triggered a switch between the smectic A and nematic phases of the 8CB (Figure S8b, Supporting Information),[24] resulting in a reversible activation and deactivation of the bubble transport on the LCIPS.

Additionally, past studies have reported the use of LC mesophase transitions to sense VOCs (e.g., toluene and dichloromethane).[25] In this context, we sought to investigate the behavior of bubbles containing toluene vapor on the LCIPS. After an air bubble containing toluene vapor was placed on the LCIPS, the toluene dissolved into the smectic A 8CB surface and consequently activated the bubble transport through a toluene-triggered LC phase transition, as seen in Figure 1j and Figures S6d and S8a, Supporting Information. Overall, these results demonstrate that LCIPS enable the controlled transport of gas bubbles using appropriate and desired stimuli, which has not been achieved in conventional isotropic-liquid-based SLIPS.[15]

In our second set of experiments, we sought to investigate the stability and generalizability of our 8CB-based LCIPS. First, we observed that the nematic LCIPS exhibit excellent underwater stability, with the underwater bubble transport remaining unaffected at least 30 days, as shown in **Figure 2**a. Second, the LCIPS shows excellent physical and chemical stability. Specifically, the average sliding velocity of a gas bubble remains almost constant on nematic LCIPS even after the LCIPS is subject to physical cutting or under harsh, corrosive solutions (e.g., aqueous solutions with pH ranging from 1 to 13, aqueous solutions of cationic and anionic surfactants, and artificial seawater) and in different organic solvents as shown in Figure 2b–d and Figures S9–S11, Supporting Information. Moreover, the air bubble remains stable on the smectic A LCIPS in the above harsh physical and chemical conditions, even when the LCIPS is under vibration (Figures S12 and S13 and Movie S2, Supporting Information). Third, our LCIPS can be prepared using a variety of substrates with different chemical natures (e.g., metal, polymers and fibers) and various shapes (e.g., serpentine, arch shape, Y-shape, and the curved surface of glass vials), as shown in Figure 2e and Figure S14, Supporting Information. We note here that all of these substrates exhibited performance identical to LCIPS-coated glass substrates for the manipulation of underwater gas bubbles. Hence, we believe that the outstanding long-term durability, excellent physical and chemical stability, and generalizability are beneficial to the potential applications of LCIPS.

As described earlier, the ability to manipulate both the adhesion and release of gas bubbles is another key requirement for the design of functional surfaces. Therefore, in our next set of experiments, we sought to investigate the effect of the LC mesophase on the adhesion and release of bubbles on LCIPS. We determined the maximum adhesion force between the gas bubble and the LCIPS by measuring the maximum volume of

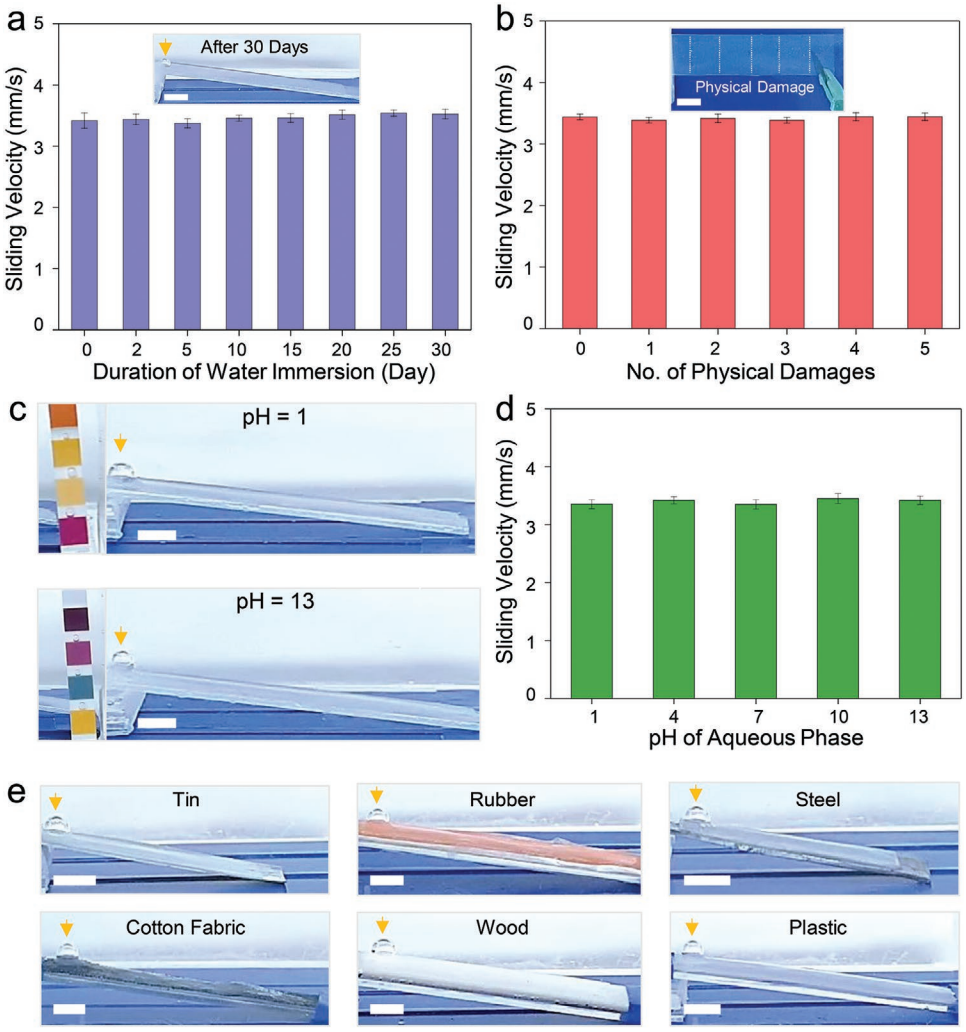

Figure 2. Generalizability and stability of LCIPS. a) Mobility of air bubbles on nematic phase LCIPS after submersion underwater for 30 days. The inset photograph is of a bubble sliding on the nematic LCIPS after 30 days of water immersion. b) Average sliding velocity of bubbles on a nematic LCIPS with damage caused by a knife. The inset photograph shows an LCIPS with multiple physical damages. c,d) Gas bubble transport on nematic LCIPS in an aqueous solution with different pH values with representative photographs (c) and a plot of their average sliding velocities (d). e) Photographs of air bubbles on nematic LCIPS coated on a variety of substrates. The yellow arrows indicate the position of the bubbles on the LCIPS. The bubble volume was 10 µL and the tilting angle was 5°. Scale bars = 5 mm.

a gas bubble that could be immobilized on the LCIPS when submerged horizontally before the spontaneous detachment of the bubble. Based on **Figure 3**a, the maximum adhesion force of a bubble on a smectic A LCIPS (30 °C) is estimated to be ≈340 µN, higher than the ≈190 µN of a nematic LCIPS (35 °C), as summarized in Figure 3b and Figure S15, Supporting Information. The corresponding adhesion force per unit length of contact line is ≈61 µN mm^{-1} for a 40 µL air bubble on smectic A LCIPS, and ≈41 µN mm^{-1} for a 25 µL air bubble on nematic LCIPS (Figure S16, Supporting Information, for the estimation of the base radius of the air bubbles). In contrast, the maximum adhesion force of an air bubble on a 20 cSt silicone-oil-based SLIPS was constant (≈190 µN; ≈38 µN mm^{-1}) in the temperature range between 25 and 45 °C. We reason here that the buoyancy force acting on the gas bubble is countered by the adhesion force from the LCIPS, which is caused by the pinning force from the receding contact line, as shown in Figure 3c. When the buoyancy force of the bubble exceeds the maximum adhesion force, it overcomes the pinning force and releases from the LCIPS. To provide insight into the role of the different LC mesophases of LCIPS, we balanced the buoyancy force of the maximum bubble volume at an LCIPS and the static friction force induced by the receding contact line:

$$\Delta\rho g V_{\text{critical}} = 2\pi r\left(\gamma_{\text{w-LC}} + \gamma_{\text{v-LC}}\right)\sin\theta_{\text{Rec}} \tag{2}$$

where V_{critical} is the minimum volume of a single air bubble that detaches from the LCIPS. Based on Equation (2), we estimated the θ_{Rec} of bubbles on LCIPS to be ≈155° and ≈161° for the smectic A and nematic phases, respectively. To provide additional support, we measured the adhesion force of air bubbles with different volumes on smectic A and nematic LCIPS using a Kruss-tensiometer-based micro-electromechanical balance system (Supporting Information). For example, the adhesion

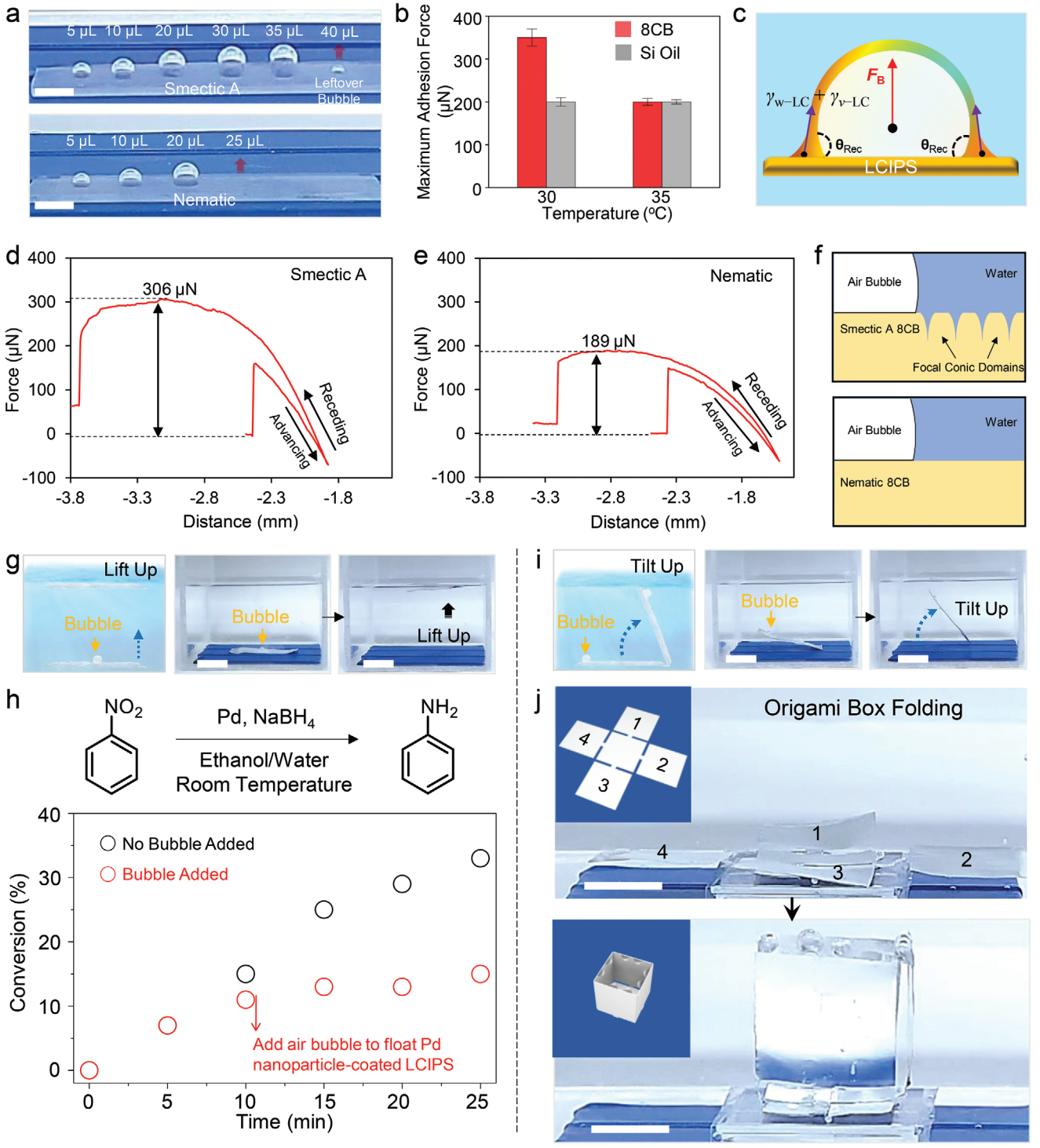

Figure 3. Adhesion and release of bubbles on LCIPS. a) Photographs of air bubbles with different volumes on a horizontal LCIPS in smectic A (30 °C) and nematic phases (35 °C). b) Maximum adhesion force of LCIPS and silicone-oil-based SLIPS. c) Schematic illustration showing the dominating forces during bubble release on LCIPS. d,e) Force of air bubbles on smectic A (d) and nematic (e) LCIPS. f) Schematic illustration of the surface roughness of smectic A and nematic LCIPS. g) Smectic A LCIPS-coated aluminum foil lifted up using gas bubbles. h) Bubble-induced termination in the hydrogenation of nitrobenzene by raising a Pd-nanoparticle-decorated aluminum foil coated with smectic A LCIPS. i) Smectic A LCIPS-coated aluminum foil tilting up using gas bubbles. j) Schemes and corresponding photographs of origami box folding driven by the adhesion of multiple bubbles on a smectic A LCIPS. The bubble volume was 20 μL. Scale bars = 5 mm.

force of 15 µL air bubbles was measured to be 306 ± 2 µN (≈69 µN mm^{-1}) on smectic A LCIPS surface and 189 ± 2 µN (≈48 µN mm^{-1}) on nematic LCIPS, as shown in Figure 3d,e, and in the Supporting Information. Our force measurement validates our observations that the smectic A LCIPS exhibits an ≈62% higher adhesion force compared to that of nematic LCIPS, which provides opportunities for control over the adhesion and release of air bubbles on LCIPS. It is well established that surface roughness significantly affects the pinning of the contact lines at the surface and thus the CAH.[26a,b] Previous research has reported that the surface roughness of nematic 8CB is on the order of angstroms,[26c] whereas depressions caused by focal conic domains[26d] increase the surface roughness of smectic A 8CB to the order of nanometers and higher, as shown in Figure 3f. We hypothesize that the intrinsically high surface roughness of smectic A LCIPS causes a more severe pinning of air bubbles at its surface compared to nematic LCIPS, resulting in a higher adhesion force of air bubbles on smectic A LCIPS (see detailed discussion in Supporting Information).

Based on the above observations of the LC-mesophase-dependent bubble adhesion, we explored the possibility of using air bubbles pinned to LCIPS for object locomotion. We immersed a 55 mg LCIPS-coated piece of aluminum foil with dimensions of 30 mm × 10 mm in an aqueous solution of $NaHCO_3$ and then injected HCl (1 M) to generate CO_2 in situ on the LCIPS. As shown in Figure S17, Supporting Information, large bubbles would not adhere to a nematic LCIPS, causing the LCIPS to remain fully submerged. In contrast, larger CO_2 bubbles readily adhered to the LCIPS when the 8CB was in the smectic A phase. Afterward, the resulting buoyancy force overpowered the gravitational force causing the LCIPS to float to the top of the water surface, as shown in Figure 3g and Movie S3, Supporting Information. Based on this finding, we demonstrate that we can use bubble adhesion to manipulate the floating of smectic A LCIPS-coated aluminum foil decorated with palladium (Pd) nanoparticles on top surface of the aluminum foil to control the rate of a catalytic reaction, for example, the hydrogenation of nitrobenzene (Figure 3h and Materials and Methods in Supporting Information). The combination of the controlled vertical movement and position-dependent chemical reactivity is similar to the behaviors exhibited by various aquatic microorganisms.[3] Furthermore, the gas bubble-driven locomotion of smectic A LCIPS was observed to depend on the position of the CO_2 bubble generation. As shown in Figure 3i, when the CO_2 bubble was generated close to one edge of the smectic A LCIPS, that edge of the LCIPS was observed to tilt up from the edge with the attached bubbles. Building on this observation, we further demonstrate that even a sophisticated manipulation of objects underwater, such as folding a box in an origami manner, can be achieved through bubble adhesion on the LCIPS, as shown in Figure 3j.

Building upon the controllability of gas bubble transport and adhesion, we sought to design an LCIPS-based bubble gating system in the final set of experiments, which can selectively "open" and "close" using external stimuli. As shown in **Figure 4**a, in the smectic A phase (25 °C), the 15 µL air bubbles remained pinned on the LCIPS surface, rendering the LCIPS bubble gate closed. Upon heating to the nematic phase (35 °C), the LCIPS gate opened, allowing the bubbles to slide on both sides and subsequently merge into a single 30 µL bubble, which was then released from the top of the LCIPS (Figure S19 and Movie S4, Supporting Information). This behavior is analogous to an electronic circuit logic "AND" gate, where the bubble gate being open and closed corresponds to "TRUE" and "FALSE" Boolean variables, respectively. To explore the potential application of our LCIPS-based bubble gating system, we first developed LCIPS that not only sense VOCs in air bubbles but, more importantly, separate VOC-containing bubbles from pure air bubbles. As shown in Figure 4b, when a pure air bubble was introduced from the inlet, the bubble detached from the smectic A LCIPS and was released from compartment 1. In contrast, when an air bubble contaminated by a VOC was introduced, the VOC locally triggered the smectic A–nematic phase transition, resulting in the sliding of the VOC-containing air bubble on the tilted LCIPS and a subsequent detachment into compartment 2. Furthermore, this prototype device can efficiently sense and sort air bubbles based on VOC contamination for more than 600 successive bubbles, as shown in Figure 4c, and were shown to detect VOC concentrations as low as ≈7 parts per million (ppm). We note here that this functionality is generalizable to other common organic chemical vapors including chloroform and dichloromethane.

Second, we explored the potential use of LCIPS in the manipulation of oxygen levels in cell cultures. While hypoxic solid tumor microenvironments (0.5–5 vol% of oxygen) in cancer patients significantly promote tumor progression and therapeutic resistance,[27] the vast majority of in vitro tumor cell cultures have been conducted in ambient air with an extra-physiological oxygen tension (21 vol%). Chemical induction,[28a] microfabricated devices,[28b] 3D spheroid cultures,[28c] and hypoxic incubators and chambers[28d,e] have been widely used to create hypoxic conditions in cell cultures, although these approaches require expensive or specialized equipment. To obtain in vivo hypoxic conditions, we used LCIPS to regulate the oxygen level in normal cell cultures in vitro, as shown in Figure 4d (see Materials and Methods in Supporting Information). When the LCIPS was in the nematic phase, the nitrogen bubbles were transported to the cell culture to achieve the desired low oxygen level, resulting in the decomposition of tirapazamine (TPZ; a hypoxia-responsive antitumor pro-drug) and the subsequent death of a variety of tumor cells (e.g., A549 lung tumor, U87MG glioblastoma, and MDA-MB-231 breast tumor) under hypoxic conditions, as shown in Figure 4e,f and Figure S20, Supporting Information. In contrast, when the LCIPS was in the smectic A phase, the tumor cell culture was exposed to ambient air condition, leading to a high viability of the tumor cells, as shown in Figure 4g. In addition, we have shown that the oxygen level can be regulated through manipulation of the LC mesophases to tune the cancer cell viability. Our results demonstrate that our LCIPS enable precise control of oxygen levels in cell cultures (Figure 4h,i), providing a novel platform to mimic in vivo hypoxic conditions.

3. Conclusion

The results reported in this work reveal various key functionalities and intrinsic characteristics of our newly designed LCIPS,

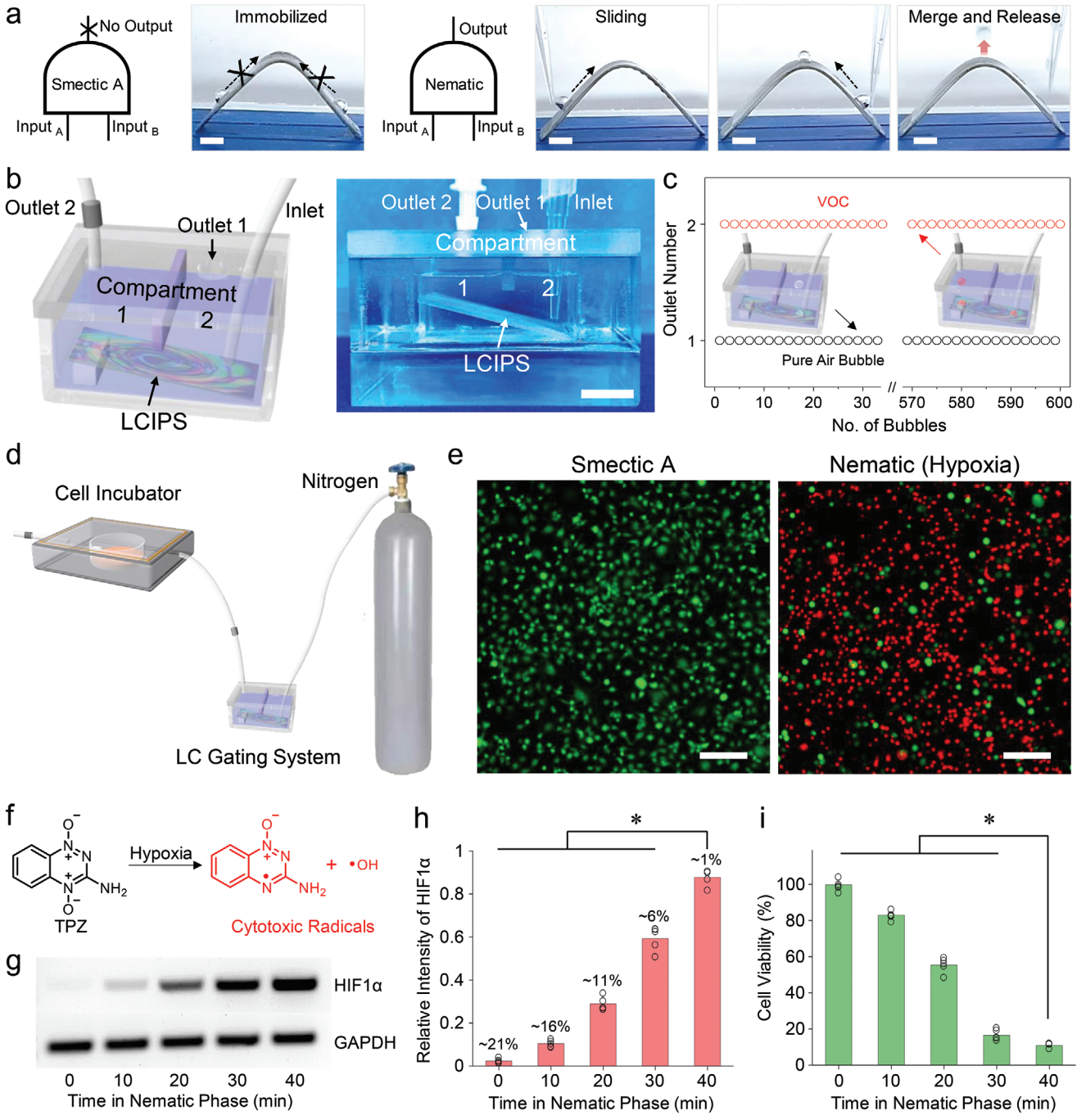

Figure 4. Design of an LCIPS-based gas bubble gating system. a) Schemes and corresponding photographs of the bubble-based gating system as analogous to an electronic circuit logic "AND" gate. Each bubble volume was 15 µL. Scale bars = 5 mm. b) Schematic illustration and photograph of a prototype LCIPS-based gas bubble gating device. Scale bar = 1 cm. c) Plot showing the reusability of the LCIPS-based gas bubble gating device to sense and sort VOC-contaminated bubbles from pure air bubbles. The pure air bubble (transparent) is released into compartment 1 and the VOC-contaminated air bubble (red) is released into compartment 2. d) Schematic illustration and photograph of the experimental setup of an LCIPS bubble gate to manipulate oxygen levels in cell cultures. e) Generation of cytotoxic radicals via decomposition of tirapazamine (TPZ) under hypoxic conditions. f) Live (Calcein AM)/dead (propidium iodide) cell staining of U87MG glioblastoma cells treated with 20 µg mL^{-1} of TPZ for 24 h using an LCIPS bubble gate in different LC phases. Scale bar = 200 µm. g) Reverse transcription PCR (RT-PCR) analysis and h) quantification of hypoxia-inducible factor 1-alpha (HIF1α) expression in U87MG cells as a function of time the LCIPS was in the nematic phase prior to cell incubation. Glyceraldehyde-3-phosphate dehydrogenase (GAPDH) was used as a control. The mole fraction of oxygen in the gas phase of cell incubation is labeled in (h). i) Cell viability assessment of U87MG cells treated with 20 µg mL^{-1} of TPZ for 24 h as a function of time the LCIPS was in the nematic phase prior to cell incubation. Data are represented as mean standard deviation of five independent replicates ($p < 0.05$).

including LC-mesophase-dependent adhesion between the air bubbles and the LCIPS. Assisted by buoyancy forces, the sliding and pinning of air bubbles on LCIPS can be reversibly switched through the manipulation of the LC mesophase transition. Importantly, this LCIPS system presents opportunities for achieving an unprecedented level of multi-stimuli-responsiveness and functionalities using gas bubbles, including cyanobacteria-inspired object movement and smart catalysis. More importantly, the LCIPS was further explored as a bubble gating device to sense and sort VOC-contaminated bubbles and obtain an in vivo hypoxic microenvironment for tumor biology studies and the development and screening of new drugs. In addition, this LCIPS system exhibits outstanding long-term underwater stability, exceptional physical and chemical durability, and generalizability to a variety of substrates.

Overall, these results demonstrate that LCIPS offer a new class of responsive and multifunctional surfaces with programmable mobility of gas bubbles that could benefit various applications, including microreactors, smart bubble delivery, and effective therapeutic discovery. In particular, because of the characteristic multi-stimuli-responsiveness and functionalities, LCIPS may provide significant advantages over previously explored superhydrophobic surfaces and isotropic-liquid-based SLIPS. Finally, we note that the results presented in this work suggest several directions for future research, including further research into the interaction of gas bubbles with LC surfaces in different phases (e.g., cholesteric, blue phase, and chiral smectic).

Supporting Information

Supporting Information is available from the Wiley Online Library or from the author.

Acknowledgements

A.M.R., Y.X., and Y.C. contributed equally to this work. The authors would like to thank Robert K. A. Bennett for helpful discussion. The authors also thank Michael Wilson from the Machine Shop in Department of Chemical and Biomolecular Engineering at The Ohio State University (OSU) for his help with device fabrication. This work was supported by startup funds from OSU, OSU Institute for Materials Research Kickstart Facility Grant, Davidson School of Chemical Engineering, and the College of Engineering at Purdue University. The authors also gratefully acknowledge Robbers New Investigator support from the Purdue University Center for Cancer Research, P30CA023168, Purdue Institute for Integrative Neuroscience (PIIN) and Bindley Biosciences Center, and the Walther Cancer Foundation.

Conflict of Interest

The authors declare no conflict of interest.

Data Availability Statement

The data that support the findings of this study are available from the corresponding author upon reasonable request.

Keywords

gas-bubble adhesion, gas-bubble transport, liquid crystals, lubricated surfaces, stimuli responsive materials

Received: December 11, 2021
Revised: January 23, 2022
Published online: February 24, 2022

[1] O. S. George, *Nature* **1953**, *171*, 885.
[2] R. S. Seymour, P. G. D. Matthews, *J. Exp. Biol.* **2013**, *216*, 164.
[3] a) C. S. Reynolds, R. L. Oliver, A. E. Walsby, *N. Z. J. Mar. Freshwater Res.* **1987**, *21*, 379; b) A. E. Walsby, *Microbiol. Rev.* **1994**, *58*, 94; c) J. Huisman, G. A. Codd, H. W. Paerl, B. W. Ibelings, J. M. H. Verspagen, P. M. Visser, *Nat. Rev. Microbiol.* **2018**, *16*, 471.
[4] a) A. Agarwal, W. J. Ng, Y. Liu, *Chemosphere* **2011**, *84*, 1175; b) T. Azuma, K. Otomo, M. Kunitou, M. Shimizu, K. Hosomaru, S. Mikata, Y. Mino, T. Hayashi, *Sep. Purif. Technol.* **2019**, *212*, 483; c) Z. Xia, L. Hu, *Water* **2019**, *11*, 55; d) X. Xiong, B. Wang, W. Zhu, K. Tian, H. Zhang, *Catalysts* **2019**, *9*, 10.
[5] a) E. C. Ungera, T. Porterc, W. Culpd, R. Labella, T. Matsunagaa, R. Zutshi, *Adv. Drug Delivery Rev.* **2004**, *56*, 1291; b) C. Francesca, Z. Meifang, A. k. Muthupandian, *Curr. Top. Med. Chem.* **2010**, *10*, 1198; c) K. Chen, E. Chaung, S. Wey, K. Lin, F. Cheng, C. Lin, H. Liu, H. Tseng, C. Liu, M. Wei, *ACS Nano* **2014**, *8*, 5105; d) J. Shao, M. Xuan, L. Dai, T. Si, J. Li, Q. He, *Angew. Chem., Int. Ed.* **2015**, *54*, 12782.
[6] a) S. Chang, T. Si, S. Zhang, M. A. Merrick, D. E. Cohn, R. X. Xu, *Ultrason. Sonochem.* **2016**, *28*, 31; b) F. H. L. Aaron, M. A. Borden, P. A. Dayton, D. E. Kruse, S. I. Simon, K. W. Ferrara, *J. Controlled Release* **2006**, *111*, 128.
[7] A. K. Balasubramanian, A. C. Miller, O. K. Rediniotis, *AIAA J.* **2004**, *42*, 411.
[8] a) G. H. Seo, G. Jeun, S. J. Kim, *Int. J. Heat Mass Transfer* **2016**, *102*, 1293; b) A. Mehralizadeh, S. R. Shabanian, G. Bakeri, *Therm. Sci. Eng.* **2020**, *15*, 100451.
[9] X. Zhang, Y. Dong, Z. He, H. Gong, X. Xu, M. Zhao, H. Qin, *ACS Appl. Mater. Interfaces* **2020**, *12*, 18174.
[10] R. Ma, J. Wang, Z. Yang, M. Liu, J. Zhang, L. Jiang, *Adv. Mater.* **2015**, *27*, 2384.
[11] C. Zhang, M. Cao, H. Ma, C. Yu, K. Li, C. Yu, L. Jiang, *Adv. Funct. Mater.* **2017**, *27*, 1702020.
[12] a) C. Shi, X. Cui, X. Zhang, P. Tchoukov, Q. Liu, N. Encinas, M. Paven, F. Geyer, D. Vollmer, Z. Xu, H. J. Butt, H. B. Zeng, *Langmuir* **2015**, *31*, 7317; b) W. Barthlott, T. Schimmel, S. Wiersch, K. Koch, M. Brede, M. Barczewski, S. Walheim, A. Weis, A. Kaltenmaier, A. Leder, H. F. Bohn, *Adv. Mater.* **2010**, *22*, 2325.
[13] a) T. S. Wong, S. H. Kang, S. K. Y. Tang, E. J. Smythe, B. D. Hatton, A. Grinthal, J. Aizenberg, *Nature* **2011**, *477*, 443; b) X. Yao, Y. H. Hu, A. Grinthal, T. S. Wong, L. Mahadevan, J. Aizenberg, *Nat. Mater.* **2013**, *12*, 529; c) Q. Wei, C. Schlaich, S. Prevost, A. Schulz, C. Bottcher, M. Gradzielski, Z. H. Qi, R. Haag, C. A. Schalley, *Adv. Mater.* **2014**, *26*, 7358; d) U. Manna, D. M. Lynn, *Adv. Mater.* **2015**, *27*, 3007; e) D. C. Leslie, A. Waterhouse, J. B. Berthet, T. M. Valentin, A. L. Watters, A. Jain, P. Kim, B. D. Hatton, A. Nedder, K. Donovan, E. H. Super, C. Howell, C. P. Johnson, T. L. Vu, D. E. Bolgen, S. Rifai, A. R. Hansen, M. Aizenberg, M. Super, J. Aizenberg, D. E. Ingber, *Nat. Biotechnol.* **2014**, *32*, 1134; f) J. B. Boreyko, G. Polizos, P. G. Datskos, S. A. Sarles, C. P. Collier, *Proc. Natl. Acad. Sci. USA* **2014**, *111*, 7588; g) X. Zhang, L. Sun, Y. Wang, F. Bian, Y. Wang, Y. Zhao, *Proc. Natl. Acad. Sci. USA* **2019**, *116*, 20863; h) Y. Long, X. Yin, P. Mu, Q. Wang, J. Hu, J. Li, *Chem. Eng. J.* **2020**, *401*, 126137;

i) K. Han, L. Heng, Y. Zhang, Y. Liu, L. Jiang, *Adv. Sci.* **2019**, *6*, 1801231.

[14] a) R. Togasawa, M. Tenjimbayashi, T. Matsubayashi, T. Moriya, K. Manabe, S. Shirator, *ACS Appl. Mater. Interfaces* **2018**, *10*, 4198; b) J. Yang, J. Li, X. Jia, Y. Li, H. Song, *ACS Appl. Mater. Interfaces* **2020**, *12*, 28645. c) X. Jing, Z. Guo, *Nanoscale* **2019**, *11*, 8870.

[15] a) C. Yu, X. Zhu, K. Li, M. Cao, L. Jiang, *Adv. Funct. Mater.* **2017**, *27*, 1701605; b) Y. Jiao, X. Lv, Y. Zhang, C. Li, J. Li, H. Wu, Y. Xiao, S. Wu, Y. Hu, D. Wu, J. Chu, *Nanoscale* **2019**, *11*, 1370; c) X. Lv, Y. Jiao, S. Wu, C. Li, Y. Zhang, J. Li, Y. Hu, D. Wu, *ACS Appl. Mater. Interfaces* **2019**, *11*, 20574; d) C. Zhang, B. Zhang, H. Ma, Z. Li, X. Xiao, Y. Zhang, X. Cui, C. Yu, M. Cao, L. Jiang, *ACS Nano* **2018**, *12*, 2048; e) X. Wang, H. Bai, J. Yang, Z. Li, Y. Wu, C. Yu, L. Jiang, M. Cao, *Small* **2021**, *17*, 2007803; f) X. Wang, Z. Wang, L. Heng, L. Jiang, *Adv. Funct. Mater.* **2020**, *30*, 1902686; g) X. Xiao, C. Zhang, H. Ma, Y. Zhang, G. Liu, M. Cao, C. Yu, L. Jiang, *ACS Nano* **2019**, *13*, 4083.

[16] a) P. Guo, Z. B. Wang, L. P. Heng, Y. Q. Zhang, X. Wang, L. Jiang, *Adv. Funct. Mater.* **2019**, *29*, 1808717; b) K. Han, K. Yong, *Adv. Funct. Mater.* **2021**, *31*, 2101970; c) J. Zhang, P. Liu, B. Yi, Z. Wang, X. Huang, L. Jiang, X. Yao, *ACS Nano* **2019**, *9*, 10596; d) Y. Jiao, Y. Zhang, X. Lv, J. Ji, Z. Wang, Y. Su, X. Liu, K. Liu, *Langmuir* **2021**, *6*, 2140; e) Y. Zhang, Y. Jiao, C. Chen, S. Zhu, C. Li, J. Li, Y. Hu, D. Wu, J. Chu, *Langmuir* **2019**, *35*, 10625; f) S. Zhu, Y. Bian, T. Wu, C. Chen, Y. Jiao, Z. Jiang, Z. Huang, E. Li, J. Li, J. Chu, Y. Hu, D. Wu, L. Jiang, *Nano Lett.* **2020**, *20*, 5513.

[17] a) Z. Huang, C. Chen, X. Wang, R. Li, Y. Bian, S. Zhu, Y. Hu, J. Li, D. Wu, J. Chu, *ACS Appl. Mater. Interfaces* **2021**, *13*, 9272; b) C. Chen, Z. Huang, L.-A. Shi, Y. Jiao, S. Zhu, J. Li, Y. Hu, J. Chu, D. Wu, L. Jiang, *Adv. Funct. Mater.* **2019**, *29*, 1904766.

[18] a) C. M. Paleos, D. Tsiourvas, *Angew. Chem., Int. Ed.* **1995**, *34*, 1696; b) R. S. Zola, H. K. Bisoyi, H. Wang, A. M. Urbas, T. J. Bunning, Q. Li, *Adv. Mater.* **2019**, *31*, 1806172; c) D. Y. Kima, K. U. Jeong, *Liq. Cryst. Today* **2019**, *28*, 34; d) K. Nayani, P. Rai, N. Bao, H. Yu, M. Mavrikakis, R. J. Twieg, N. L. Abbott, *Adv. Mater.* **2018**, *30*, 1706707; e) L. Zhang, S. Maity, K. Liu, Q. Liu, R. Göstl, G. Portale, W. H. Roos, A. Herrmann, *Small* **2017**, *13*, 1701207; f) P. P. Muhoray, *Phys. Today* **2007**, *60*, 54.

[19] a) C. Chang, H. Kuo, K. Tang, S. Chiu, *Appl. Phys. Lett.* **2011**, *99*, 073504; b) W. Zhang, D. Fan, Y. Gong, W. Liang, *Liq. Cryst.* **2021**, *48*, 1643; c) M. B. Pantoja, Y. Yang, N. L. Abbott, *Liq. Cryst.* **2019**, *46*, 1925.

[20] a) X. Wei, N. Sbalbi, L. C. Bradley, *Soft Matter* **2020**, *16*, 9121; b) Y. Luo, D. A. Beller, G. Boniello, F. Serra, K. J. Stebe, *Nat. Commun.* **2018**, *9*, 3841; c) E. Bukusoglu, X. Wang, Y. Zhou, J. A. Martınez-González, M. Rahimi, Q. Wang, J. J. de Pablob, N. L. Abbott, *Soft Matter* **2016**, *12*, 8781; d) N. V. Solodkov, J. Shim, J. C. Jones, *Nat. Commun.* **2019**, *10*, 198; e) Y. K. Kim, J. H. Noh, K. Nayani, N. L. Abbott, *Soft Matter* **2019**, *15*, 6913; f) J. Kołacz, A. Konya, R. L. B. Selinger, Q. H. Wei, *Soft Matter* **2020**, *16*, 1989.

[21] a) P. Popov, E. K. Mann, A. Jákli, *J. Mater. Chem. B* **2017**, *5*, 5061; b) A. Sen, K. A. Kupcho, B. A. Grinwald, H. J. V. Treeck, B. R. Acharya, *Sens. Actuators, B* **2013**, *178*, 222; c) Y. Han, K. Pacheco, C. W. M. Bastiaansen, D. J. Broer, R. P. Sijbesma, *J. Am. Chem. Soc.* **2010**, *132*, 2961; d) C. Esteves, E. Ramou, A. R. P. Porteira, A. J. M. Barbosa, A. C. A. Roque, *Adv. Opt. Mater.* **2020**, *8*, 1902117; e) K. D. Cadwell, N. A. Lockwood, B. A. Nellis, M. E. Alf, C. R. Willis, N. L. Abbott, *Sens. Actuators, B* **2007**, *128*, 91; f) M. L. Bungabong, P. B. Ong, K.-L. Yang, *Sens. Actuators, B* **2010**, *148*, 420.

[22] M. Škarabot, E. Osmanagič, I. Muševič, *Liq. Cryst.* **2006**, *33*, 581.

[23] Y. Xu, A. M. Rather, Y. Yao, J.-C. Fang, R. S. Mamtani, R. K. A. Bennett, R. G. Atta, S. Adera, U. Tkalec, X. Wang, *Sci. Adv.* **2021**, *7*, 7607.

[24] E. Bukusoglu, M. B. Pantoja, P. C. Mushenheim, X. Wang, N. L. Abbott, *Annu. Rev. Chem. Biomol. Eng.* **2016**, *7*, 163.

[25] a) W. Hu, J. Sun, Q. Wang, L. Zhang, X. Yuan, F. Chen, K. Li, Z. Miao, D. Yang, H. Yu, H. Yang, *Adv. Funct. Mater.* **2020**, *30*, 2004610; b) N. Akamatsu, K. Hisano, R. Tatsumi, M. Aizawa, C. J. Barrett, A. Shishido, *Soft Matter* **2017**, *13*, 7486;

[26] a) M. Miwa, A. Nakajima, A. Fujishima, K. Hashimoto, T. Watanabe, *Langmuir* **2000**, *16*, 5754; b) W. Choi, A. Tuteja, J. M. Mabry, R. E. Cohen, G. H. McKinley, *J. Colloid Interface Sci.* **2009**, *339*, 208; c) M. Sadati, H. Ramezani-Dakhel, W. Bu, E. Sevgen, Z. Liang, C. Erol, M. Rahimi, N. T. Qazvini, B. Lin, N. L. Abbott, B. T. Roux, M. L. Schlossman, J. J. de Pablo, *J. Am. Chem. Soc.* **2017**, *139*, 3841; d) M. J. Gim, D. A. Beller, D. K. Yoon, *Nat. Commun.* **2017**, *8*, 15453.

[27] Y. Ando, H. P. Ta, D. P. Yen, S. S. Lee, S. Raola, K. Shen, *Sci. Rep.* **2017**, *7*, 15233.

[28] a) D. Wu, P. Yotnda, *J. Visualized Exp.* **2011**, *54*, 2899; b) C. P. Thomas, S. R. Raghavan, S. P. Forry, *Anal. Chem.* **2011**, *22*, 8821; c) D. R. Grimes, C. Kelly, K. Bloch, M. Partridge, *J. R. Soc., Interface* **2014**, *11*, 20131124; d) R. Wang, F. Jin, H. Zhong, *Am. J. Cancer Res.* **2014**, *1*, 53; e) S. Saxena, I. Agrawal, P. Singh, S. Jha, *Med. Devices Sens.* **2020**, *3*, 10064.